Subproject C3.2

Frequency and Time-Domain Electronic Spectroscopy of Isolated Clusters and Carbon Nanotubes

Principle Investigators: Manfred M. Kappes, Andreas-Neil Unterreiner

Further Scientists:
Dr. Artur Böttcher, Dr. Oliver Hampe[a], Dr. Detlef Schooss[a], Dr. Frank Hennrich[a], Dr. Sergei Lebedkin[a], Dr. Patrick Weis

Institut für Physikalische Chemie
Karlsruher Institut für Technologie (KIT), Campus Süd

[a]Institut für Nanotechnologie
Karlsruher Institut für Technologie (KIT), Campus Nord

Introduction and Summary

Subproject C3.2 is concerned with the characteristic interactions of molecular nanostructures with light and with the modulation of such interactions as a result of external perturbations ideally controllable at the single molecule level. A focus of the work in the previous project period has been on decay processes following electronic excitation. These include electron loss, light emission and photofragmentation. Knowledge and control of such processes (rates and branching ratios) is of potential relevance for the use of the corresponding species in single nanostructure photonic and opto-electronic devices. We have pursued an approach in which *the same systems* are studied both in the frequency and time domain. Furthermore, we try to sort out the role of the local environment by studying trapped, mass selected ions under ultrahigh vacuum conditions in addition to *the same* chromophores within a condensed phase matrix or at interfaces. So far we have probed primarily single walled carbon nanotubes (SWNTs) and fullerenes as model systems because these nanocarbon systems allow facile control of particle size, geometric/ electronic structure and charge state. We have also begun analogous work on other emitter systems such as silicon nanoparticles as well as semiconductor cluster complexes.

Measurements on SWNTs have encompassed nIR photoluminescence spectroscopy of semiconducting SWNTs as well fsec time-resolved pump-probe transient absorption measurements thereof. We have developed methods, which allow for photoluminescence (PL) and Raman spectromicroscopy of single SWNTs in the frequency domain. Results include the quantification of matrix dependent spectral shifts and their dependence on chiral index, the observation that free-standing defect-free SWNTs do not show PL blinking and the first direct experimental study of dark excitonic states in SWNTs. In addition we have studied changes to individual SWNT electronic properties as a result of (local) strain and torsion. An important component of the spectroscopic work on nanotube systems has encompassed the fractionation of SWNT materials according to length, diameter, electronic structure type and most recently chiral index – for which new high throughput separation methods were developed (and studied).

1. Frequency-domain spectroscopy of SWNTs

1.1 Experimental setup and nanotube samples

Characterization of individual emitting (semiconducting) SWNTs was carried using a home-built near-infrared PL laser microscope [C3.2:11]. The microscope incorporates tunable cw lasers for excitation in the spectral range of ~610-1000 nm, a cooled InGaAs photodiode array for detection in the range of ~800-1600 nm, and a computer-controlled x-y-z piezo-driven stage for sample scanning and PL imaging. Resonant Raman spectroscopy and imaging of SWNTs has been performed using a commercial Raman microscope (model CRM200, WiTec GmbH Ulm). The routine lateral spatial resolution of the Raman and PL microscopes is about 300 and 400 nm, respectively. Recently, we have developed and built an optical filter module for Raman microscopy, incorporating novel ultra-narrow holographic notch filters for low-frequency Raman spectroscopy and imaging which allows detection of Raman signals down to ~10/20 cm^{-1} in Stokes/anti-Stokes shift. This module essentially provides a very high rejection of the elastically scattered (i.e. Rayleigh scattered) laser excitation light by a factor of ~10^{11} and thus allows simultaneous acquisition of remaining Rayleigh as well as Stokes and anti-Stokes Raman signals practically for any sample [C3.2:60]. Currently, we are also developing a polarisation-modulation Rayleigh imaging microscope with the aim to provide a fast 'visualisation' of individual nanotubes.

Various SWNT samples have been used in these studies, including nanotubes grown by catalytic chemical vapor deposition (CVD) on different substrates and in different geometries in our group [C3.2:2] [C3.2:11] as well as in the group of Prof. Yan Li in a cooperation with Peking University. Complementary to *single* nanotube studies which have primarily made use of CVD grown tubes, we have extensively employed frequency-domain spectroscopy (absorption, Raman and FTIR-PL [1]) for characterisation of *ensembles* of dispersed SWNTs in aqueous and organic solutions. In particular, PL measurements of (*n,m*)-narrowed SWNT dispersions, i.e. enriched in only one or a few specific nanotube (*n,m*)-structures, have provided valuable insight into photophysical properties of SWNTs [C3.2:24] (see section **2**). Such dispersions were also a starting material for dielectrophoretic deposition of nanotubes onto electrode microstructures (collaboration with R. Krupke (B1.9, C4.1)) and for ultrafast time-domain spectroscopy experiments (see section **3**). For SWNT dispersions, we have mostly used SWNT materials produced in the gas phase either by the HiPco method (from Carbon Nanotechnologies, Inc.) or by the pulsed laser evaporation method [2] from our laboratory. In the following, some of the recent spectroscopic results are described in more detail.

1.2. PL imaging and AFM manipulation of millimeter-long carbon nanotubes

Arrays of aligned, individual, millimeter-long CVD carbon nanotubes grown horizontally on Si/SiO_2 substrates (Fig. 1) appear to be an optimal configuration for many proposed SWNT sensor applications. We have shown that PL microscopy can be applied as a versatile method to characterize semiconducting (emitting) nanotubes in such arrays [C3.2:40]. To obtain both spectroscopic and topographic information for the same nanotubes, we have combined PL and atomic force microscopy. The arrays of SWNTs used in these studies were produced at Peking

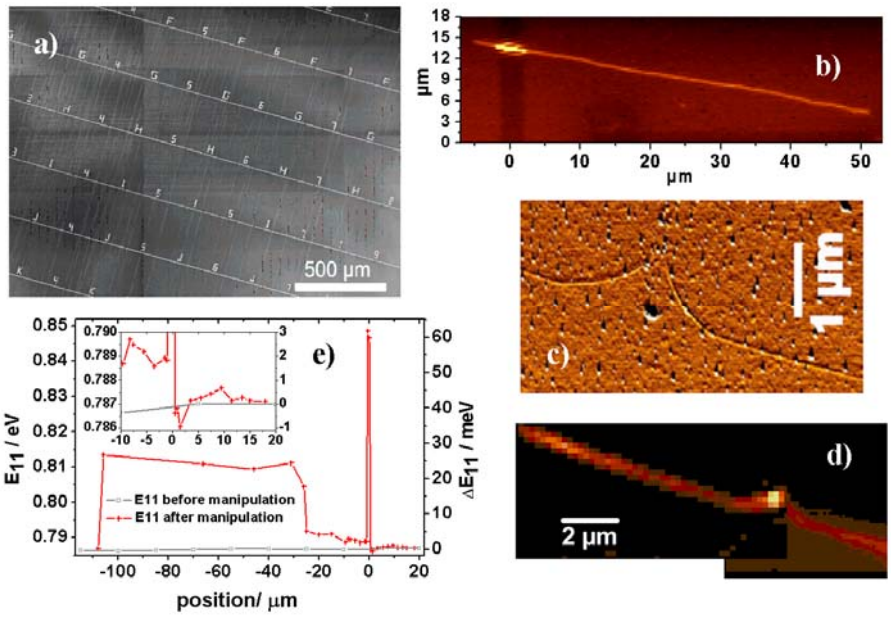

Fig. 1: (a) SEM image of an array of mm-long SWNTs grown on a microstructured Si/SiO_2 substrate (from Ref. 3). Long white lines correspond to 3.5 µm wide and 0.5 µm trenches etched on the substrate. (b) micro-PL image of a nanotube assigned to (12,4)-species. The bright emission spot is related to a tube section suspended over the trench. (c) AFM and (d) PL images of a (15,2)-nanotube fractured by dragging an AFM tip perpendicular to the tube axis, and (e) profile of the PL emission energy along the nanotube. Position 0 corresponds to the fracture site.

university on prefabricated microstructured substrates also comprising markers for reliable identification and positioning of nanotubes (Fig. 1a) [3]. Due to the μm-wide trenches etched on the substrates, two different local surroundings for the same nanotubes could be compared – air-suspended nanotube segments across the trenches versus on-SiO_2 segments.

Fig. 1b shows a typical PL image of a nanotube piece – the air-suspended segment appears as a short bright stripe due to ~10-20 times larger PL intensity relative to on-SiO_2 segments. In addition, the PL emission (E_{11}) and excitation (E_{22}) energies (obtained from PL maps like those presented in Fig. 2C,D) are red-shifted by up to ~10-25 meV for on-SiO_2 segments. This can be explained by the screening effect of the SiO_2 substrate (see below). Furthermore, the uniformity of a nanotube (*n,m*)-structure can be checked by PL profiling, i.e. by acquiring PL maps at different locations along the nanotube. The PL is also quite sensitive to mechanical strain in the nanotubes via characterisitic shifts of the E_{11} and E_{22} energies. We have found that micromanipulation of nanotubes on a substrate with an AFM tip (dragging, curving, fracturing, etc.) results in siginificant residual deformation of the nanotubes. This is illustrated by the emission energy profile in Fig. 1e indicating residual axial and torsional strain around the fracture site in such an AFM-manipulated nanotube (Fig. 1c,d). A particularly interesting situation results when AFM micromanipulation ('rolling') induces mostly torsional strain in a nanotube. In this case, PL profiling across the manipulation site can determine the handedness of this luminescent (=chiral) nanotubes via the very characteristic E_{11} and E_{22} shifts pattern [C3.2:40].

1.3. PL microscopy of vertically-aligned carbon nanotube arrays

Fig. 2 shows typical scanning electron microscopy (SEM) images of vertically-aligned arrays or 'forests' of carbon nanotubes. They have been grown by CVD, typically from ethylene at 700°C, on different substrates such as sapphire, silicon and quartz, each covered with nanometer-thick layers of iron catalyst and alumina [C3.2:11]. 'Forests' of up to ~1 mm height (~nanotube length) could be grown within ~90 min. Typically, ~2-10 nm thick multiwalled carbon nanotubes were the major fraction in these samples. By comparison, the SWNTs also present were grown at a relatively low density, within a broad diameter range, and frequently found to be overhanging on the top of the 'forests'. Therefore, the latter were not only interesting carbon nanotube materials, but were also found to be valuable samples for PL and Raman microscopy of air-suspended, i.e. 'surroundings-free', nanotubes.

We have measured PL maps of over 250 individual air-suspended SWNTs in carbon nanotube 'forests' and have thus accurately determined E_{11} (emission) and E_{22} (excitation) energies for over 20 (*n,m*)-species (Fig. 2C, D). These energies for individual SWNTs in air (vacuum) could then be correlated with those in other einvironments. They were found to be blue-shifted by a few tens of meV relative to their counterparts in water-surfactant dispersions (Fig. 2E) [4] [C3.2:11]. This could be explained to first approximation by the external dielectric screening effect on electronic excitations (excitons) in nanotubes. The observed blue-shifts of E_{11} and E_{22} energies for SWNTs in air/vacuum, i.e. in the absence of external screening, agrees qualitatively well with theoretical predictions [5]. An accurate quantitative theoretical description of the screening effect in SWNTs is, however, still challenging. Interestingly, in water-surfactant dispersions, SWNTs are screened with an effective dielectric constant of $\varepsilon_{eff} \approx 2.3$, i.e. with a similar ε_{eff} value or with PL shifts comparable to those found for nanotubes in organic media such as toluene or paraffine oil. This similarity between aqueous and organic environments can be rationalized as a result of the dynamic character of the screening of short-lived excitons in SWNTs (on the time scale of picoseconds) and their fast diffusion (over tens of nm) along SWNTs [C3.2:11].

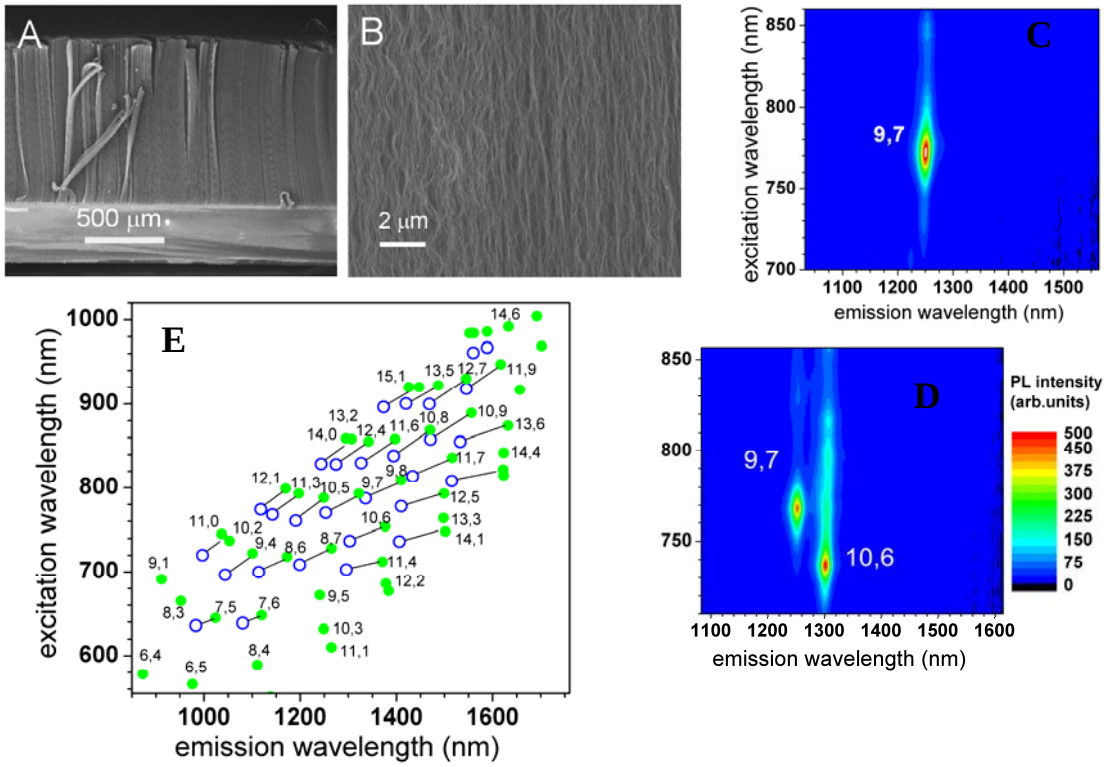

Fig. 2: (A, B) SEM side images of a ~1 mm high carbon nanotube 'forest' grown by CVD on a silicon substrate. (C, D) Typical PL maps (color-coded emission intensity versus emission and step-scanned excitation wavelengths) of individual (*n,m*)-nanotubes suspended at low density on the top of the 'forest'. (E) Correlation between excitation and emission wavelengths (optical transition energies) of air-suspended (*n,m*)-nanotubes and those in a water-surfactant dispersion (open blue and closed green circles, respectively).

1.4. PL blinking in SWNTs

Light emission of single molecules and quantum dots, in particular at low temperatures, often reveals temporal fluctuations in intensity and spectral position, called PL blinking. This effect has been observed in different systems and can hinder their application at the single emitter limit. The blinking has often been attributed to a fluctuating charge trapping in the surrounding matrix or substrate, resulting in an appearance of efficient non-radiative recombination channels. The experimental verification is, however, challenging, since the environment can only be poorly controlled in most molecular (quantum dot) systems studied. Individual SWNTs deposited on a substrate from dispersions, i.e. SWNTs coated with surfactant molecules, also demonstrate PL blinking, in particular at temperatures below ~20 K [6]. To elucidate a possible role of the surroundings (surfactant molecules and/or substrate), we have compared the low-temperature PL of individual nanotubes deposited from dispersions with that of air-suspended, 'surrounding-free' nanotubes on top of the carbon nanotube 'forests' (see Fig. 2 A and B). In agreement with Ref. 6, PL blinking was observed for all detected surfactant-coated nanotubes. In contrast, stable PL was observed for all emitting suspended nanotubes (Fig. 3). These results demonstrate that PL blinking

is not an intrinsic property of SWNTs (and likely of many other molecular systems), but is caused by interaction with the nanotube surroundings [C3.2:18].

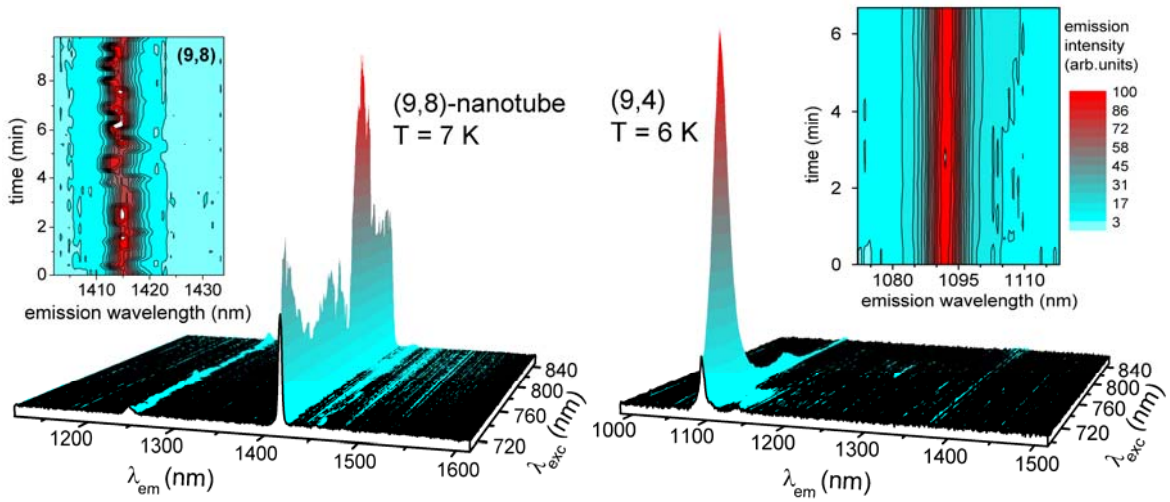

Fig. 3: Low-temperature 3D PL maps (color-coded emission intensity versus emission and excitation wavelengths) measured for two individual SWNTs: deposited on sapphire from a water-surfactant dispersion (left) and found on top of a CVD-grown carbon nanotube 'forest' (right). The insert maps (2D contour plots) show time evolution of the PL emission peak over timescales of several minutes.

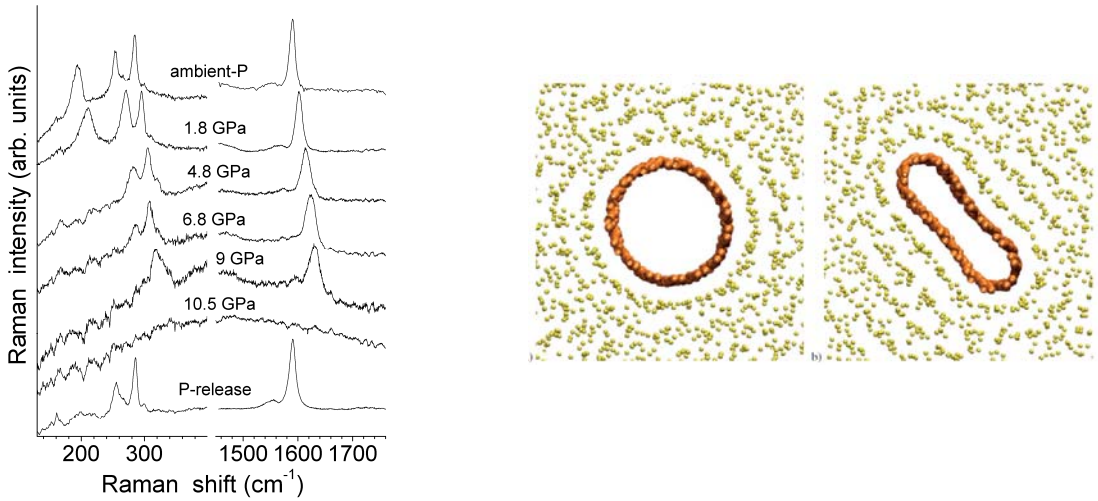

Fig. 4: Raman spectra of individually dispersed SWNTs under high hydrostatic pressure. The disappearance of the charactersitic Raman bands at some critical pressure is attributed to the nanotube collapse as illustrated by molecular dynamics simulation pictures (from Ref. 7) on the right side.

1.5. Radial collapse of SWNTs under high hydrostatic pressure

An interesting phenomenon is expected upon loading SWNTs with an increasing hydrostatic pressure – i.e. their radial collapse as illustrated in Fig. 4. Such collapse has been predicted in several theoretical studies to occur at a critical pressure of a few GPa, depending on the nanotube diameter (see, e.g., [7]). This critical pressure is an important parameter which is related to the general behavior of SWNTs under very high mechanical load. Early experimental studies of nanotubes under high pressure yielded, however, rather controversial results. This may be attributed to the highly inhomogeneous character of raw SWNT samples (with SWNTs aggregated in large bundles) used in those studies. We have applied Raman and PL spectroscopy to individually dispersed (*debundled*) SWNTs having diameters of d ~0.8–1.3 nm and have subjected them to compression up to 10.5 GPa in a diamond anvil cell. An 'abrupt' disappearance of the characteristic Raman signals of nanotubes – as expected for the collapse transition - was observed at 10 and 4 GPa pressure for nanotubes with d ~0.8–0.9 and ~1.2-1.3 nm, respectively (Fig. 4). These results are in a good accord with theoretical predictions [C3.2:4].

2. Chemical and physical fractionation of SWNTs

Common features of the raw materials resulting from the numerous methods developed up to date for the growth of single-walled carbon nanotubes (SWNTs) are the broad bundle size-, length-, diameter- and roll-up angle distributions (defined by chiral indices (n, m)) generated, as well the extensive byproducts such as metal catalyst particles, fullerenes and various forms of amorphous carbon. Such inhomogeneity is a serious drawback for many potential applications of nanotubes. Consequently, there is much scope for research into separation/fractionation, a direction which we have intensively pursued in the past project period. Various methods of purification separation and techniques of SWNTs have been actively investigated/established including purification via polyacylation of as-prepared SWNTs (in collaboration with T. S. Balaban (C3.5)) [C3.2:7], size separation of SWNTs via size exclusion chromatography (SEC) [C3.2:3] [C3.2:42], diameter separation via density gradient ultracentrifugation (DGU) [C3.2:20] [C3.2:38] [C3.2:49] and dielectrophoresis (in collaboration with R. Krupke (B1.9, C4.1) [8, C3.2:15]. In the following, some of more recent developments in chemical and physical fractionation/sorting of single walled carbon nanotubes (SWNTs) are described in detail. For this a short excursion into the electronic and geometric structure of SWNTs is first necessary.

The "molecular" structure of a carbon nanotube is typically related to graphene, which is a single layer of sp^2-bonded carbon atoms in a honeycomb lattice. SWNT diameters typically range between 0.5 nm and 2 nm depending on the synthesis method (our in house pulsed laser vaporization SWNT synthesis produces tubes with diameter of ~ (1 ± 0.2) nm [2]) whereas length can vary over several orders of magnitude (from 10 nm to 1 cm). The length can be important for some applications, but the electronic properties of a SWNT depend primarily on the direction in which the graphene was rolled up to form a seamless cylinder. SWNT rollup direction can be defined by a pair of integers (n, m). A typical SWNT raw soot contains up to ~ 60 different (n, m)-species of which approximately 67% of SWNTs are semiconducting and 33% are metallic at room temperature [4].

2.1. Aqueous suspensions in standard surfactants

Powerful ultrasonication is a crucial step in preparation of aqueous and organic dispersions of exfoliated (debundled) SWNTs. We have been able to demonstrate that this process results in scission of nanotubes into shorter pieces, down to a typical minimal length of ~100 nm [C3.2:10]. Sonication treated dispersions can then be length-fractionated by size exclusion chromatography

(SEC) for which appropriate protocols have been developed [C3.2:3]. Length selected fractions have been used by us for various spectroscopic studies.

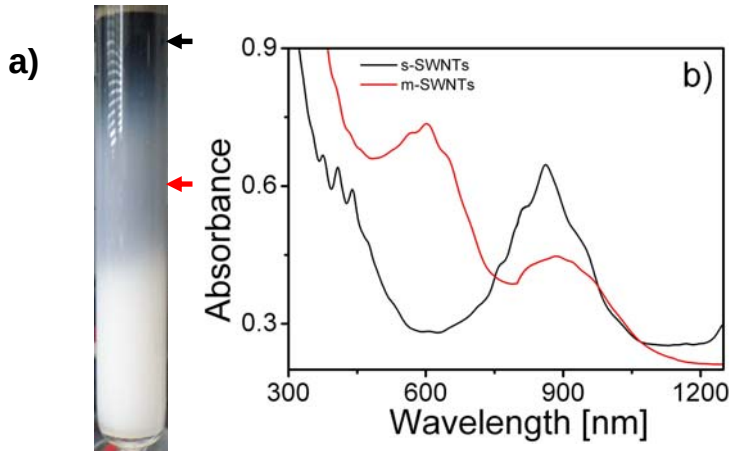

Fig. 5: (a) Photograph taken after adding of the starting suspension to the SEC medium. The m-SWNTs immediately start to propagate through the SEC medium whereas the s-SWNTs become stuck within the first few cm (indicated by red and black arrows, respectively); (b) UV vis NIR spectra of the eluted SEC fractions obtained after column separation of the starting suspension using first an eluant of 1 wt% of SDS in water (red) and subsequently an eluant of 1 wt% of SChol (black).

Widespread electronic applications of SWNTs would be greatly facilitated by the routine provision of samples fractionated by electronic structure type in a simple process. For this reason, separation of m- from s-SWNTs has become a flourishing subfield in the SWNT fractionation area and in fact enrichment of m/s-SWNTs has been achieved by various techniques including ac-dielectrophoresis [8], density gradient centrifugation [9] and agarose gel dc-electrophoresis [10] – albeit with relatively modest throughput. All such separation methods make use of nanotube/surfactant suspensions in liquids. Most commonly, aqueous suspensions with surfactants such as sodium dodecyl sulfate (SDS), sodium dodecylbenzene sulfonate (SDBS) or sodium cholate (SChol) have been used. Corresponding separation protocols all start with the preparation of suspensions enriched in "individualized" (i.e., debundled/exfoliated) tubes - typically by means of sonication treatment followed by centrifugation. We have recently shown that gel filtration/size exclusion chromatography allows high throughput separation of m- from s-SWNTs when using aqueous sodium dodecyl sulphate (SDS) suspensions (Fig. 5) [C3.2:42] – *without a prior centrifugation step.* Size exclusion chromatography (SEC) is known to separate nanoscale objects passing through a column according to differences in their size and has been extensively used to size-separate SWNTs. In this sense the observation of *m- vs. s*-SWNTs separation using size exclusion chromatography methods was unexpected. It turns out that the method relies on the initial dispersion/sonication step, which itself is already selective with respect to electronic structure type. In fact, aqueous SDS starting suspensions obtained after sonication of SWNT raw soot were found to contain s-SWNTs primarily in the form of small bundles whereas metallic SWNTs were predominantly suspended as individual tubes. With gel filtration, the bundles can then be separated from the individual tubes simply on the basis of differences in their size - by choosing an appropriate SEC column medium, particle size, gel porosity and eluant composition. In this approach the SEC column medium is used as a "filter" to trap the longer, rigidly bundled s-SWNTs, whereas the smaller individualized m-SWNTs elute as expected for regular SEC. Specifically, for

high throughput m/s-SWNT separation, the starting SWNT suspension is first loaded onto the column and then partly eluted with 1 wt. % of SDS in water. This removes the shorter (individualized) metallic tubes whereas bundled s-SWNTs remain trapped. The latter are then also removed by changing the eluant from 1 wt. % SDS in H_2O to 1 wt. % SChol in H_2O - whereupon the trapped semiconducting bundles partially dissolve and completely elute. We have applied for a corresponding patent and KIT is presently negotiating licensing of the separation method with several companies.

Equilibrium density-gradient ultracentrifugation (DGU) is an established method to separate solutes on the basis of their buoyant density [9]. Gradients and media are chosen such that the objects to be separated have a density between the highest and lowest values generated. We have exploited a DGU separation of SWNTs in surfactant- or DNA-water dispersions [C3.2:20] [C3.2:58] [C3.2:59] [C3.2:49]. The buoyant density of SWNTs in aqueous solutions might be expected to be inversely proportional to their diameter. However, surfactant, hydration layers and water filling inside nanotubes result in a very non-trivial (*n, m*)-equilibrium along a density gradient [C3.2:20] [C3.2:49]. Our results on the nanotube equilibria in density gradients strongly suggest that water molecules can indeed fill SWNTs in "standard" water-surfactant dispersions [C3.2:20] [C3.2:49]. These nanotubes have lengths of several hundreds of nanometers and likely open ends as a consequence of the dispergation (sonication) procedure. In order to interpret this experimental data, extensive molecular dynamics (MD) simulations of the energetics of water@SWNT@surfactant aggregates, the relative contributions of the surfactant and hydration layers, and, finally, the buoyant density have been performed (in cooperation with W. Wenzel; C5.1) [C3.2:20] [C3.2:49].

2.2. Polymer wrapping in organic solvents

Taking into account technical costs associated with multi-step separation methods, it is obvious that the simplest strategy would be to selectively disperse and retain just the desired SWNT species. Certain fluorene-based polymers can in fact efficiently stabilize individual nanotubes in toluene [11, 12]. Moreover, the toluene-polymer dispersions show a high selectivity towards semiconducting vs. metallic nanotubes as well as a selectivity to specific semiconducting nanotube structures. These are typically (*n, m*)-nanotubes with (n - m) = 1 and 2, i.e., with a large chiral angle, θ, close to that of metallic (*n ,n*)-nanotubes (θ = 30°). Correspondingly, this group of nanotubes could be dispersed with a high enrichment relative to other (*n, m*)-species.

We have shown that by further optimization of the dispersing and centrifuging procedure and, especially, the concentration ratios of the polymer and precursor SWNT material it is possible to obtain near monochiral nanotube samples, in a single sonication and centrifugation step without any additional treatment. In this way we have obtained (7, 5), (7, 6), (10, 5) and (9, 7) nanotubes with enrichments of ~60-90% as estimated from the optical absorbance and photoluminescence spectra (Fig. 6) [C3.2:41]. These results support the interpretation, that polymer wrapping is specific not only to a certain chiral angle, but also to a nanotube diameter. In order to further expand the number of available (*n, m*)-selected or (*n, m*)-narrowed organic dispersions of SWNTs, we have also explored for the first time density gradient centrifugation of SWNT polymer suspensions in organic solvents – specifically for nanotubes in chlorobenzene with tribromotoluene (TBT) as a density gradient forming additive [C3.2:41]. Ongoing work along these lines in collaboration with M. Mayor (C3.8) and C. Barner-Kowollik includes systematically varying substituents [C3.2:61] and polymer lengths in order to study their influence on the observed selectivity.

The ((*n,m*)-narrowed) dispersions were also used as a starting material for work in other CFN subprojects: e.g. dielectrophoretic deposition and transport measurements through nanotubes on

electrode microstructures (cooperation with R. Krupke (B1.9, C4.1)), assessment of the nanotoxicology of dispersed SWNTs (cooperation with the D. Marko (E1.1) and coupling of SWNTs to silicon slot waveguides (cooperation with J. Leuthold (A4.4)).

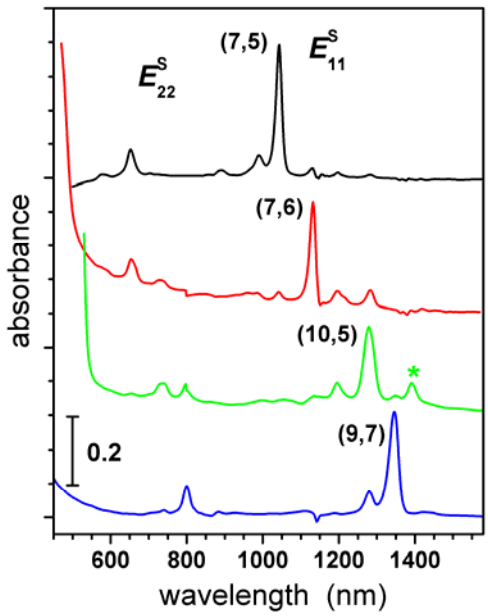

Fig. 6: Absorbance spectra of various (*n, m*)-selected dispersions of SWNTs. The spectra were measured in a 10 mm cuvette against toluene solutions of the corresponding dispersing polymers. E_{11}^S and E_{22}^S denote characteristic optical transitions in semiconducting nanotubes. The spectra are vertically shifted for clarity. The feature indicated with an asterisk is due to incomplete subtraction of the corresponding POF-BT polymer absorption.

3. Ultrafast spectroscopy of semiconducting SWNTs

Pump-probe studies of ultrafast relaxation dynamics after electronic excitation have been used to investigate specific properties of s-SWNTs. The time-resolved pump-probe spectroscopy setup used, consisted of two independently tunable, non-collinear optical parametric amplifiers and covered a spectral range of 500 to 1600 nm with a time resolution of 50 fs. Control of the wavelengths was achieved by using optical-fiber coupled near-infrared and visible detectors with a resolution of 1 - 2 nm. The laser system was optimized to allow the measurement of signal amplitudes as low as 10 µOD. Typically, < 100 µOD resolution was achievable in a day-to-day operation without additional alignment. The establishment of this technique was a prerequisite to monitor the low-amplitude response of SWNTs in the NIR region especially at wavelengths beyond 1400 nm. Purity of the samples is one of the most important issues in determining intrinsic SWNTs optical properties. Consequently, extensive use was made of various fractionated samples as described in the previous section.

Here, we present the results of studies on mixed samples with chiral vectors (6,4) and (6,5) as well as near monodispersed samples of (9,7) SWNTs in solution. In both systems, G-phonon coupled electronic excitation into the first excited state, E_{11}, was observed; in addition, in the latter case, dark state population was recorded in real-time.

3.1. Relaxation dynamics in mixtures of (6,4) and (6,5) SWNTs

The relaxation dynamics of individualized (6,5) SWNTs and mixtures of (6,4)/(6,5) SWNTs were compared in order to identify possible interaction pathways between different tube types. For this, the corresponding samples were probed in the near-infrared (NIR) spectral region after E_{11}-excitation. While resonant excitation and probing at 990 nm (primarily (6,5)-tube contribution) revealed identical transients, clear differences were observed after G-phonon assisted excitation corresponding to a pump wavelength of 860 nm (see Fig. 7). Apparently, the transient response of the mixed sample is suppressed either by overlapping of higher state absorption and emission or by exciton annihilation. Shifting the probe wavelengths slightly to the red makes this even more evident.

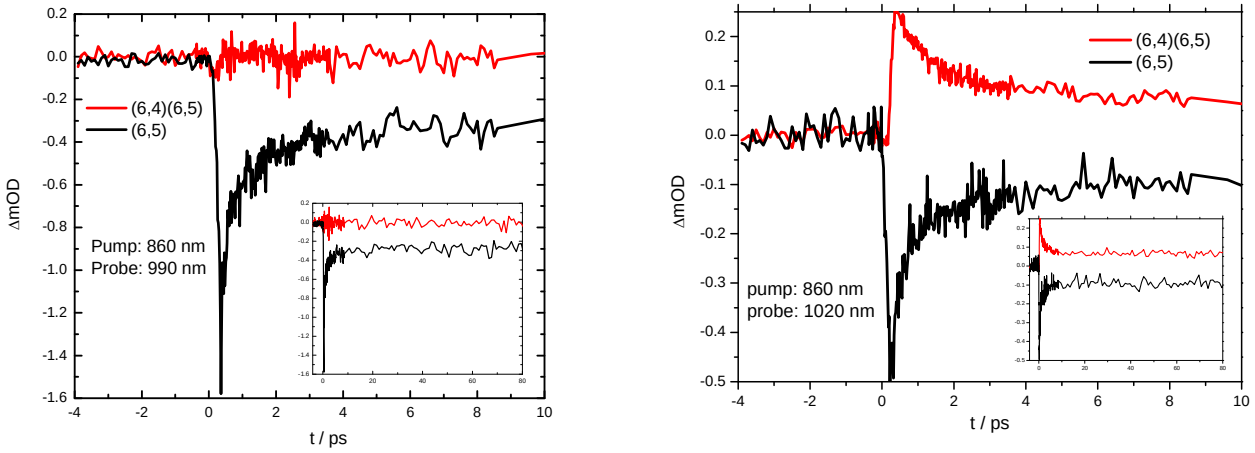

Fig. 7: Transient profiles of (6,5) and mixtures of (6,4)/(6,5) SWNTs at pump/probe wavelengths as indicated.

3.2. Dark state and phonon-assisted transitions in (9,7) SWNTs

Time-resolved one- and two- color pump-probe experiments on semiconducting (9,7)-SWNTs, dispersed in POF/toluene, yielded new insights into the relaxation pathways of the first allowed exciton state, E_{11}. The near monodispersed SWNT-suspension allowed a more accurate determination of the ~30 ps excited state lifetime than previously possible (see left Fig. 8). Further near-infrared investigations allowed the direct observation of dark state population in the vicinity of the first bright exciton state, E_{11} (right Fig. 8). Depending on probe wavelengths, the dark state(s) are observed within 1 ps after excitation. Further investigations under non-resonant conditions clearly showed the existence and an upper limit (60 fs) for the timescale of the coupling of phonon-assisted transitions of the E_{11} state.

Direct time-resolved results for DE-dynamics are generally difficult to interpret because bright-to-dark state excitation via one-photon absorption is usually not allowed and subsequent relaxation is non-radiative. Due to this difficulty the nature of these states still, remains unclear. Theoretical calculations predict the existence of at least one dark singlet exciton below E_{11} in SWNTs [13-15]. In agreement with Zhao et al. [15,16], Kilina et al. [17] have predicted three dark singlet excitonic states lying below the first bright singlet state. These could serve as trap states within the E_{11}-

manifold. Furthermore low-energy emission bands about 130 meV below E_{11} in different tubes have been detected using photoluminescence spectroscopic methods and attributed to K-momentum dark excitons energetically slightly above E_{11} [18,19]. Other experimental findings have associated this feature to dark singlet excitonic states [C3.2:14]. Depending on sample preparation, chiral index and experimental technique, further studies have provided evidence for either subdiffusive trapping of dark singlet excitons [20]; dark states 130 - 150 meV below E_{11} [21] or K-momentum dark excitons [22]. Here, further efforts towards elucidation of the dark states' nature are needed.

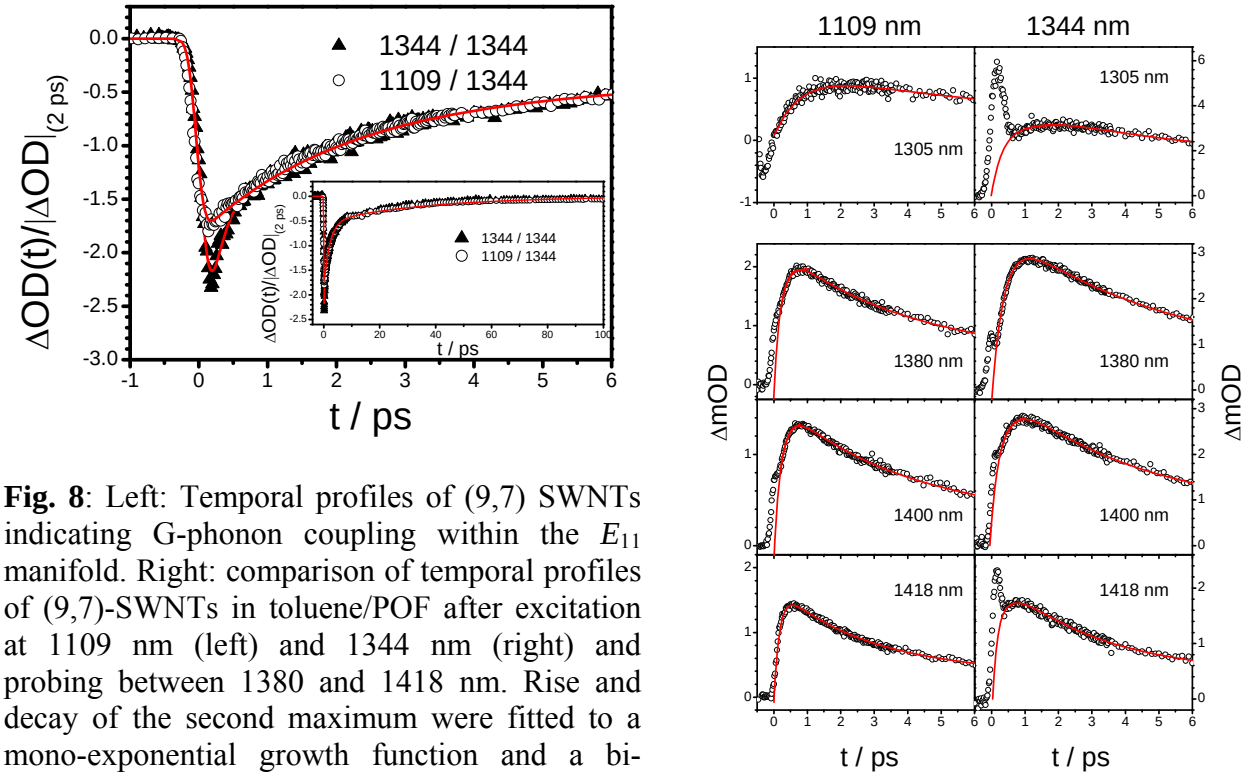

Fig. 8: Left: Temporal profiles of (9,7) SWNTs indicating G-phonon coupling within the E_{11} manifold. Right: comparison of temporal profiles of (9,7)-SWNTs in toluene/POF after excitation at 1109 nm (left) and 1344 nm (right) and probing between 1380 and 1418 nm. Rise and decay of the second maximum were fitted to a mono-exponential growth function and a bi-exponential decay function, indicated as solid lines.

4. Ultrafast spectroscopy of other molecular emitters

4.1 Direct determination of excited state lifetimes in lanthanide cluster complexes

In cooperation with C1.05 (Roesky) we have studied the ultrafast response of two tetranuclear lanthanide cluster complexes comprising Nd or Pr atoms, respectively (for structure information see Ref. [23]). Usually, access to the excited state lifetime of lanthanides by pump/probe absorption studies is cumbersome as most of the electronic transitions are quantum mechanically not allowed and only weak absorption peaks can be observed. Here, we have chosen an alternative route by making use of a ligand-to-metal charge transfer. After ultrafast excitation at 388 nm, the ligand is excited into the S_1 state (see Fig. 9) where an ultrafast (1-2 ps) intersystem crossing to the triplet state occurs. Afterwards, part of the population is subject to a ligand-metal charge transfer which is detected at certain probe wavelengths in the visible and NIR region. In all these transients a characteristic time constant of 6 ps for Nd and 26 ps for Pr compounds is found that is attributed to

the lifetime presumably of the $^4F_{3/2}$ state. From this state, fluorescence can also be observed although in quite low yields (< 0.1 %). Extensive reference measurements ruled out excess charge transfer to the solvent (MeOH) - by comparison to the ultrafast response of solvated electrons in polar media [see e.g., C3.2:53].

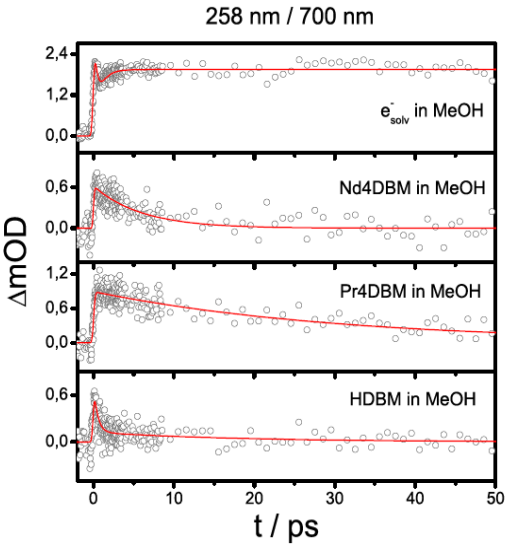

Fig. 9a: Temporal profiles of tetranuclear Nd and Pr compounds in MeOH. Top: Comparison with solvated electron, Bottom: Ligand contribution.

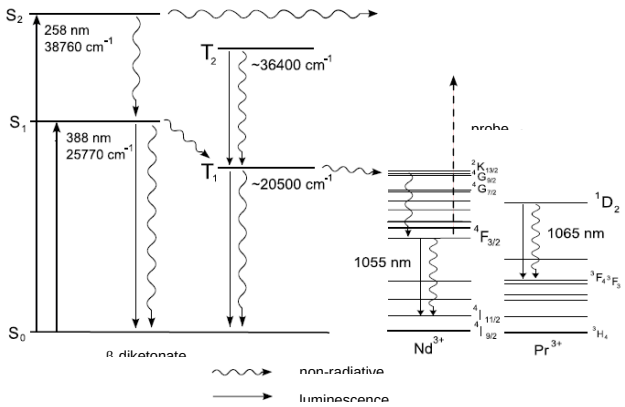

Fig. 9b: Simplified energy scheme for relaxation pathways in either Nd or Pr compounds.

4.2 Theory of transient anisotropy

Transient anisotropy can be a powerful tool in exploiting excited state properties by measuring the time-dependent change of the dipole moment of molecules. We have therefore formulated an extensive analysis of transient anisotropy including an Ansatz in the classical and semi-classical regime to describe the temporal evolution of anisotropy in multiphoton experiments in the limit of Brownian motion [Dissertation_Schalk] [C3.2:54] [C3.2:55]. This includes the derivation of the formerly unknown time evolution of many photon experiments for Brownian rotational motion based on Legendre decomposition. The non-diffusive regime could be modelled by a step model and applied to different molecular geometries. Within this model, the solvent-solute interaction shows a third order time dependence irrespective of the molecular geometry. The odd order of the interaction can be understood as a symmetry breaking term through collisions. All calculations have also been extended to multi-photon experiments.

4.3 Pseudo-rotation of the fulleride monoanion in solution

We have used probes of transient anisotropy to study excited state temporal evolution in solvated fullerene anions. The transient anisotropy (see Fig.10) decays considerably faster than the excited state population [Dissertation Brands] [24]. As transient anisotropy spectroscopy is directly sensitive to the temporal evolution of the transition dipole moment, i.e., the pump-induced change

of photo-selected molecules, one can monitor both orientational changes due to intra- or intermolecular processes. Molecular rotations usually occur on timescales from hundreds of fs up to ps and cannot be the origin of the observed fast decay. Also, anisotropy decay due to collisions with solvent molecules occurs on such (longer) timescales. Consequently, we have to postulate fast motion on the excited state surface as being responsible for this ultrafast decay. Such motions may correspond either to high frequency vibrational modes of C_{60}^- or to other processes like e.g., pseudorotations. The latter can be understood to first order as the rotation of a distortion – in our case a Jahn-Teller distortion – due to the instantaneous coupling between electronic motion and nuclear vibrations. Depending on the nature of the potential energy surfaces involved, tunnelling between different Jahn-Teller energy minima may occur instead. According to the results by Dunn et al. [25] tunnelling is of no relevance for C_{60}^- and pseudorotation is thought to be the dominant contribution here. To our knowledge, there has been so far no direct experimental evidence for such pseudorotations under room temperature conditions. From theoretical considerations, Dunn et al. [25] postulated that the time constant for pseudorotation should be 10 fs or less. Our anisotropy decay at various wavelengths may therefore be tentatively interpreted as due to pseudorotation (or at least part of it) in the first excited state – limited by the time resolution of our setup.

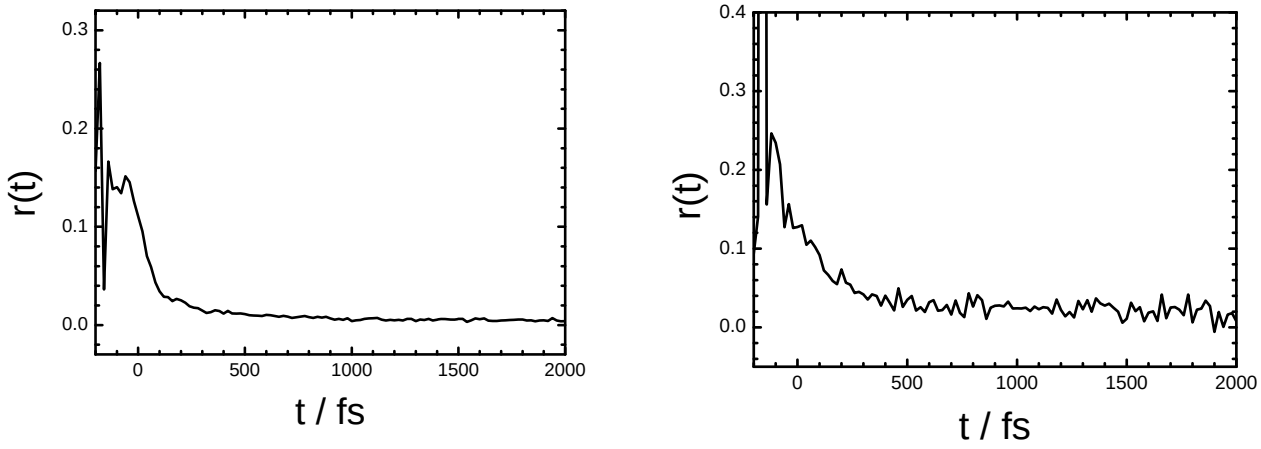

Fig. 10: Raw data of the transient anisotropy of C_{60}^- in o-dichlorobenzene at a pump/probe wavelength combination of 1070/1070 nm (left) and 950/1070 nm (right).

5. Photoelectron and photodetachment spectroscopy of isolated anions in gas-phase

Early in the project period we finished the construction of an ion beam machine containing a high intensity electrospray ion source, a time-of-flight mass spectrometer and a magnetic bottle photo-electron (PE) spectrometer. This apparatus was built to allow for time-resolved two-color photoelectron spectroscopy (TRPES) of molecular anions electrosprayed from solution and subsequently mass selected and decelerated into the detachment region of the PE spectrometer to reduce Doppler broadening prior to photoexcitation and subsequent laser detachment. The (tuneable) femtosecond laser facility used for the work in Sec. 3 was also applied for these experiments. During this project period, it was extended to allow for simultaneous measurements of transient absorption in condensed phase samples and TRPES of (other) mass selected anions. This was accomplished by upgrading the pump laser (such that pulse energies were sufficient) and by setting up a third independently tunable, non-collinear optical parametric amplifier (NOPA)

covering a spectral range of 500 – 1600 nm (with pulse durations below 50 fs), dedicated to the TRPES experiment. During the project period, research focused on fullerene anions for which the most important results are described in more detail below. In parallel to the gas-phase studies, transient absorption and transient anisotropy measurements were carried out on the same chromophores in solution. Recently, we have extended these measurements to a variety of fullerene derivatives including opened cages filled with water molecules (in a collaboration with the group of Y. Gao, Peking).

5.1 Photoelectron spectroscopy of fullerene anions: size dependent electron affinities

A prerequisite for time-resolved probes of photoinduced relaxation dynamics in fullerene mono- and dianions is knowledge of their electron affinities (EAs). Using (single photon) PE spectroscopy with ns lasers, we have determined first and second EAs of various fullerenes and their complexes. Applying our previously developed method that makes use of the organic reducing agent TDAE to generate intense ions beams of multi-anionic fullerenes, we have extended our PE experiments on fullerene dianions to the less abundant clusters C_n^{2-} with n = 88 – 96 carbon atoms. We have measured their PE spectra at detachment energies between 2 and 7 eV and determined second EAs [Dissertation_Matheis]. The new experimental data validate our previous EA[2] predictions for this size range and confirm substantial delocalization of the two unshielded excess electrons over the fullerene cage, as well as a similar extent of delocalization over the whole range of cage sizes. In a collaboration with L.-S. Wang (Richland, WA) we repeated our previous measurements of PE spectra of C_{76}^{2-}, C_{78}^{2-} and C_{84}^{2-} at ambient conditions with collisionally cooled ions at nominal 70-100 K and at higher resolution [C3.2:12]. The lower internal energies allowed determining their EA_2 values to an accuracy of 10-20 meV, validating our previously measured vertical values. Vibrationally resolved PE spectra of the colder fullerenes show that vibronic detachment channels have only weak oscillator strengths. This result from the rigidity of the fullerene cages upon charging/ discharging, as has been previously also found for electron emission of *singly* charged anions. Using our (by way of recycling HPLC) isomer enriched samples we could unambiguously assign second EAs of the two C_{2v} and the D_3 isomers of C_{78} and the D_2 and D_{2d} isomers of C_{84}. In addition to multi-anionic fullerenes, we also became interested in the PE spectroscopy of covalently linked fullerene dimers such as $C_{120}O^{2-}$ [C3.2:23]. The dianion has a second EA of 1.02 eV and its electronic ground state can be viewed as comprising two weakly coupled excess electrons, one on each on cage.

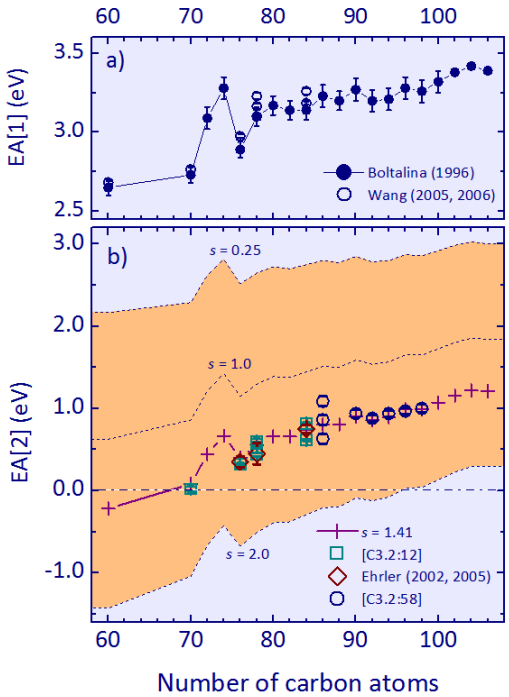

Fig. 11: Size dependent first and second electron affinities of isolated fullerenes.

5.2 Electron emission of higher fullerene dianions: mechanistic aspects

Photoinduced relaxation dynamics of fullerene dianions C_{76}^{2-} and C_{84}^{2-} were probed following visible and UV photoexcitation at 532 nm and 355 nm [C3.2:25], respectively, and infrared multi-photon absorption between 600 cm^{-1} and 1700 cm^{-1} [C3.2:43]. Despite the different excitation wavelengths, both processes lead to delayed electron emission on a millisecond timescale due to

efficient coupling of nuclear and electronic degrees of freedom. Analyzing laser fluence dependent electron yields after absorption at 532 and 355 nm, absolute absorption cross sections were determined to be 0.6-0.8 Å^2 suggesting rapid electronic relaxation by internal conversion and excess electron emission from the ground state. This process takes up most of the oscillator strength, or as a corollary, the direct photodetachment process into a continuum state though energetically accessible for 355 nm irradiation has a cross-section below 0.02 Å^2 [C3.2:1].

5.3 Femtosecond pump-probe photoelectron spectroscopy of isolated fullerene anions

We have examined ultrafast photodynamics of mass-selected C_{60}^- fullerene anions with pump/probe (775/388 nm) PE spectroscopy [C3.2:6]. The 3d-TRPES data in Fig. 12a shows measured PE spectra in the energy range of excited-state detachment as a function of pump-probe delays between -2 and 5 ps. The lowest electronically excited state decays on a 2.2±0.2 ps to the ground state. Based on DFT calculations, this is assigned to the $B(^2E_g)$ state at 1.26 eV. The prevalent de-excitation by means of internal conversion (IC) is in contrast to predominant intersystem crossing of the lowest singlet state in *neutral* C_{60}. Multivariate global fit analysis of the TRPES data (shown in Fig. 12b) reveals that C_{60}^- is initially photoexcited to a higher-lying bright state, which decays on an ultrafast timescale of <180 fs and populates the *B* state by nonradiative decay [Dissertation Rensing].

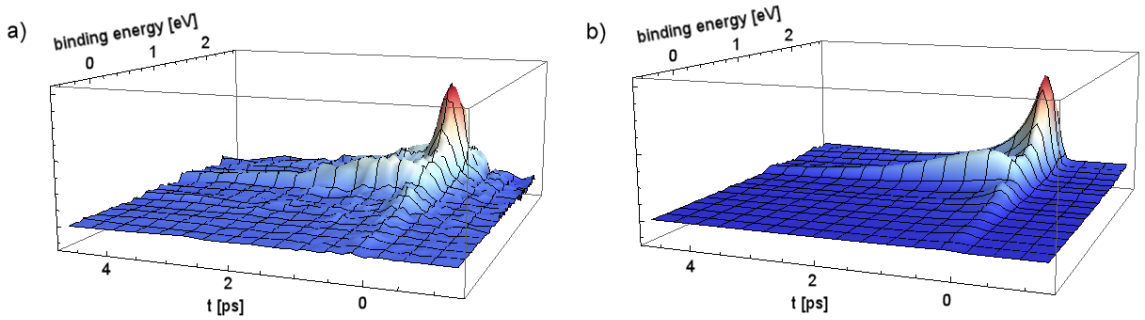

Fig. 12: Time-resolved photoelectron spectra of isolated fullerenes C_{60}^- after photoexcitation at 775 nm. The energy range is selected to predominantly visualize transient excited-state detachment, a) experiment and b) the result of the multivariate analysis.

TRPES was also performed on higher fullerene dianions C_n^{2-} with $n = 88 - 96$ following absorption at 775 nm [Dissertation_Rensing]. The initially populated excited states decay by means of ultrafast non-radiative decay and the electronic excitation is completely thermalized within 0.2 – 1 ps throughout the whole cluster size range. Relaxation timescales are indicative of de-excitation by IC, similar to C_{60}^-. However, excited-state lifetimes are shorter due to the generally lower symmetry of the larger fullerenes and their narrower HOMO-LUMO gaps that allow for faster conversion of electronic into vibrational energy. This indicates that electronic relaxation in higher fullerene dianions is dominated by the final relaxation step acting as a 'phonon bottleneck'.

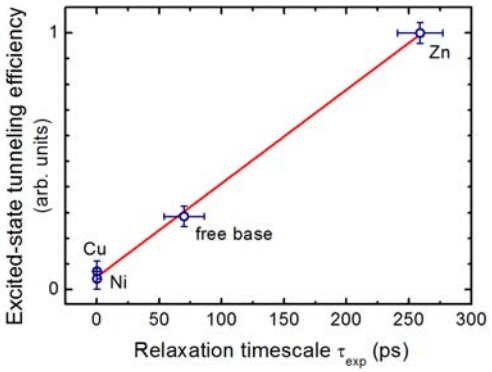

Fig. 13: Relative excited-state tunneling yield of photoexcited $[MPc(SO_3)_4]^{4-}$ MCAs correlate linearly with excited state lifetimes.

5.4 Excited state tunneling of molecular multianions

Multiply negatively charged ions (MCAs) suffer destabilization from Coulomb repulsion of the unshielded excess electrons. As a consequence, ionic fragmentation and electron autodetachment compete with other radiative and non-radiative de-excitation pathways that lower the internal energy of photoexcited MCAs. As the remaining fragments in either case are negatively charged, their interaction at large separations is dominated by electrostatic repulsion, which leads to a repulsive Coulomb barrier (RCB) at intermediate distances. We used TRPES on prototypical molecules to study picosecond photodynamics in highly unstable multi-anions following visible absorption. Phthalocyanine-tetrasulfonate tetraanions $[MPc(SO_3)_4]^{4-}$ are metastable by ~1 eV even in their electronic ground state, i.e. they undergo slow autodetachment on a timescale of seconds. We have probed their photodynamics (in compounds with M = Cu, Ni, H_2) following absorption at 775 nm in the red wing of the characteristic Q band [C3.2:19]. Excited states of the fourfold negatively charged phthalocyanines with Ni or Cu central atom decay by IC and consecutively through the various electronically excited states on a ps timescale, until all internal energy is transferred to vibrations. In contrast, "free base" (M = H_2) and ZnPc tetraanions show strong autodetachment in the excited state by tunneling of an excess electron through the RCB. Correlation of excited state tunneling yields and lifetimes gives a linear dependence, which confirms that excited state tunneling is independent of the central atom and ~12 orders of magnitude faster compared to ground state autoemission. This is in agreement with WKB rates that are determined by the similar ground state energies and geometries of the various phthalocyanine tetraanions. Pumping NiPc and the free base in the center of the Q and Q′ bands (at 600 and 660 nm, respectively) with the new tunable NOPA laser system, we found that excited state electron tunneling is independent of additional vibrational excitation [Dissertation_Rensing].

5.5 Photoinduced unimolecular ionic fragmentation in molecular multianions

We have extended TRPES of multianions to pump/probe (775/258 nm) PE spectroscopy of hexabromo-iridate(IV) dianions [C3.2:44]. While $IrBr_6^{2-}$ is electronically stable in its ground state, it is metastable with respect to emission of bromide fragment ions. However, the dissociation barrier is high enough to prevent fragmentation at ambient conditions. Photoexcitation at 775 nm shifts charge density from the halide atoms to the central metal atom. The electronic excitation decays by internal conversion in two consecutive steps with lifetimes of 2 and 20 ps and leaves the molecule hot in the ground state. Radiative cooling is too slow to efficiently stabilize the molecule and a bromide ion is emitted with a lifetime of 79 ps. This fragmentation process can be observed in the PE spectra in the form of two atomic lines resulting from detachment to the $^2P_{3/2}$ and $^2P_{1/2}$ states of Br (see Fig. 14). As the separation of the halide fragment and the anionic $IrBr_5^-$ mother ion increases, the electron affinity of the halide approaches its unperturbed value. Modeling of the unimolecular decay rate and comparison with results from DFT yields a barrier of 0.95 eV for the dissociation reaction in the electronic ground state.

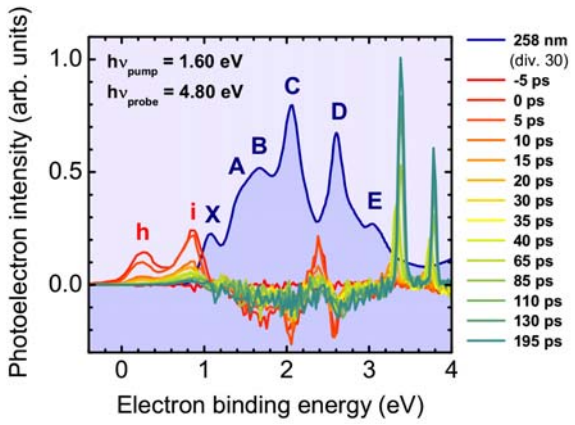

Fig. 14: Photoinduced excited-state dynamics and unimolecular fragmentation in $IrBr_6^{2-}$.

References

[1] S. Lebedkin, K. Arnold, F. Hennrich, R. Krupke, B. Renker and M. M. Kappes, New Journal of Physics **5**, 140.1–140.11 (2003).
[2] S. Lebedkin, P. Schweiss, B. Renker, S. Malik, F. Hennrich, M. Neumaier, C. Stoermer, M. M. Kappes, Carbon **40**, 417-423 (2002).
[3] Z. Jin, H. B. Chu, J. Y. Wang, J. X. Hong, W. C. Tan and Y. Li, Nano Lett. **7**, 2073 (2007).
[4] S. M. Bachilo, M. S. Strano, C. Kittrell, R. H. Hauge, R. E. Smalley, R. B. Weisman, Science **298**, 2361 (2002).
[5] T. Ando, J. Phys. Soc. Japan **66**, 1066 (1997).
[6] H. Htoon, M. J. O'Connell, P. J. Cox, S. K. Doorn, and V. I. Klimov, Phys. Rev. Lett. **93**, 027401 (2004)
[7] R. B. Capaz, C. D. Spataru, P. Tangney, M.L. Cohen and S. G. Louie, Phys. Stat. Sol. B **241**, 3352 (2004)
[8] R. Krupke, F. Hennrich, H. von Loehneysen, M. M. Kappes, Science **301**, 344 (2003).
[9] M. S. Arnold, A. A. Green, J. F. Hulvat, S. I. Stupp, M. C. Hersam, Nat. Nanotechnol. **1**, 60 (2006).
[10] T. Tanaka, H. Jin, Y. Miyata, H. Kataura, Appl. Phys. Express **1**, 114001 (2008).
[11] A. Nish, J.-Y. Hwang,J. Doig, R. J. Nicholas, Nature Nanotechnology **2**, 640 (2007).
[12] J.-Y. Hwang, A.Nish, J. Doig, S. Douven, C.-W. Chen, L.-C. Chen, R.J. Nicholas, J. Am. Chem. Soc. **130**, 3543 (2008).
[13] V. Perebeinos, J. Tersoff and P. Avouris, Nano Lett. **5**, 2495 (2005)
[14] C. D.Spataru, S. Ismail-Beigi, R. B. Capaz and S. G. Louie, Phys. Rev. Lett. **95**, 247402 (2005)
[15] H.Zhao and S. Mazumdar, Phys. Rev. Lett. **93**, 157402 (2004)
[16] H. Zhao, S. Mazumdar, C.-X. Sheng, M. Tong, and Z. V. Vardeny, Phys Rev. B **73**, 075403 (2006)
[17] S. Kilina, E. Badaeva, A. Piryatinski, S. Tretiak, A. Saxena and A. R. Bishop, Phys. Chem. Chem. Phys. **11**, 4113 (2009)
[18] O. N. Torrens, M. Zheng and J. M. Kikkawa, Phys. Rev. Lett. **101**, 157401(2008)
[19] Y. Murakami, B. Lu, S. Kazaoui, N. Minami, T. Okubo and S. Maruyama, Phys. Rev. B **79**, 195407 (2009).
[20] Z. Zhu, J. Crochet, M. S. Arnold, M. C. Hersam, H. Ulbricht, D. Resasco and T. Hertel, J. Phys. Chem. C **111**, 3831 (2007)
[21] (a) H. Harutyunyan, Tobias Gokus, A. A. Green M. C. Hersam, M. Allegrini and A. Hartschuh, Phys. Stat. Sol. B 246, 2679 (2009). (b) H. Harutyunyan, Tobias Gokus, A. A. Green M. C. Hersam, M. Allegrini and A. Hartschuh, Nano Lett. **9**, 2010 (2009)
[22] R. Matsunaga, K. Matsuda and Y. Kanemitsu, Phys. Rev. B **81**, 033401 (2010)
[23] V. Baskar and P. W. Roesky, Z. Anorg. Allg. Chem., **631**, 2782–2785 (2005)
[24] M. J. Hope, M. P. Higlett, D. L. Andrews, S. R. Meech, I. D. Hands, J. L. Dunn and C. A. Bates, Chem. Phys. Lett., **112**, 474 (2009)
[25] J. L. Dunn, I. D. Hands and C. A. Bates, J. Mol. Struct., **60**, 838 (2007)